

Controlled synthesis of Au@TiO₂ mesoporous hollow nanofibers by one-step polyethylenimine-regulated electrospinning method for efficiently photocatalytic oxidation of CO

Tianwei Dou, Yangyang Zhu, Zhanyu Chu, Lei Sun^{*}, Zhijun Li^{*}, Liqiang Jing^{*}

Key Laboratory of Functional Inorganic Materials Chemistry (Ministry of Education), School of Chemistry and Materials Science, International Joint Research Center for Catalytic Technology, Heilongjiang University, Harbin 150080, PR China

ARTICLE INFO

Keywords:

TiO₂ mesoporous hollow nanofibers
Coaxial electrospinning technique
Polyethylenimine regulation
Photocatalysis
CO oxidation

ABSTRACT

TiO₂ mesoporous hollow nanofibers with excellent mass diffusion is an attractive photocatalytic material to remove toxic gaseous pollutants like CO, while it is highly desired to improve the photogenerated charge separation and O₂ activation. Herein, the Au nanoparticles inner-loaded TiO₂ mesoporous hollow nanofibers (Au@TO MPHNFs) have been controllably fabricated by one-step coaxial electrospinning, in which it is crucial to use polyethylenimine as porogen and stabilizer for mesoporous and TiO₂ in nanofibers shell. Concurrently, a stepwise phase transfer technique is employed to realize the uniform and stable dispersion of the Au in the paraffin oil as core precursor. The Au@TO MPHNFs exhibits 2.7 and 7.4-fold CO photooxidation enhancement compared with commercial P25 and TO MPHNFs, respectively. The enhanced photoactivity can be attributed to the creation of the mesoporous hollow structure for facilitating better mass transportation, and the incorporation of Au nanoparticles for efficient charge separation and O₂ activation. Meanwhile, the photothermal effect of Au expedites intermediaries transformation and product desorption.

1. Introduction

As one of the important atmospheric pollutants, CO is widely derived from motor vehicle emissions, industrial exhaust gas and incomplete fuel combustion, etc. It poses a significant risk to human health, both in terms of acute and chronic toxicity, yet it often goes ignored due to its colorless and odorless [1,2]. Additionally, the absence of functional groups renders traditional filtration or adsorption technologies ineffective in achieving satisfactory treatment outcomes, while thermal catalysis technologies exhibit high energy consumption and are unsuitable for low concentration treatments [3,4]. Consequently, the need for the creation of environmentally friendly and safe room-temperature CO oxidative removal technologies is growing. The photocatalytic oxidation of CO with O₂ into CO₂ is considered a promising technology due to its ability to function under mild conditions without excessive energy consumption [5–7]. In this regard, TiO₂ as the most widely studied photocatalytic material acclaimed for its robust photo-oxidation capacity, cost-effectiveness and environmentally friendly nature, offers great potential for photocatalytic environmental remediation [8–10]. Moreover, the practical potential of nanofibers structured TiO₂

surpasses that of conventional nanoparticles (NPs) [11,12]. It is less prone to agglomeration, allows for easy separation and recycling, and exhibits advantages in terms of photogenerated charge separation and increased catalytic site exposure, etc [13]. However, it is meaningful to increase surface area of TiO₂ nanofibers for efficient photocatalysis.

In general, porous and hollow structures are being introduced into nanofibers to increase surface area and improve mass transfer, etc [14–16]. Usually, existing porogens such as P123 and F127, whilst able to facilitate the creation of micro and mesoporous structures, have inadequate thermal stability in terms of NPs and pore structure. Conventional porogens are often removed at low temperatures (200–300 °C), but they are far below the requirement for high crystallinity of semiconductor photocatalysts (~500 °C), while elevating temperature can cause the growth and phase change of NPs, leading to the collapse of the pore structure and subsequent detriment of photocatalytic performance [17]. Our previous studies have indicated the effectiveness of amino groups in augmenting the thermal stability of TiO₂, as it observed that amino-modified TiO₂ preserved the anatase phase after 600 °C treatment [18]. Therefore, the incorporation of porogens containing a substantial quantity of amino groups can

^{*} Corresponding authors.

E-mail addresses: 2021022@hlju.edu.cn (L. Sun), 2018011@hlju.edu.cn (Z. Li), jinglq@hlju.edu.cn (L. Jing).

<https://doi.org/10.1016/j.apcatb.2024.124112>

Received 20 January 2024; Received in revised form 6 April 2024; Accepted 22 April 2024

Available online 23 April 2024

0926-3373/© 2024 Elsevier B.V. All rights reserved.

concomitantly construct mesoporous structures and enhance the thermal stability of anatase. Polyetherimide (PEI) is an economically viable, industrially produced cationic polymer rich in amino groups, shows promise as it could interact with metal alkoxides by forming hydrogen-bonds [19,20]. Thus, it can be expected that PEI could serve as an effective porogen while improving the phase stability of TiO_2 and pore stability in nanofibers.

As well known, effective photogenerated charge separation and O_2 activation are the keys to the enhancement of the photocatalytic CO oxidation performance [21,22]. The present studies reveal that plasma metal such as Au, Ag, and Cu modified TiO_2 can significantly improve photogenerated charge separation and O_2 activation [23–26]. Among these metals, Au is more suitable due to its high stability, potent O_2 activation ability, and surface plasmon resonance (SPR) effect under visible light irradiation [27–29]. Usually, according to the spatial structure of Au- TiO_2 composites, there are three main forms: Au modified on the surface of TiO_2 , Au implanted in TiO_2 and Au@ TiO_2 core/yolk-shell structures [30]. In particular, core/yolk-shell structure is beneficial to the stability of precious metal with nano-size in the reaction process, the inner light reflection improves the utilization efficiency of the excitation light and as a nanoconfinement reactor can improve the catalytic reaction activity and selectivity, so it often shows excellent photocatalytic performance [31]. However, the current methods for synthesizing metal-oxide-coated noble metal nanocomposites with a well-controlled core-shell or yolk-shell structure predominantly rely on a relatively complicated or environmentally unfriendly process, which entail the utilization of either hard/soft templates or etching procedures involving toxic agents [32]. Therefore, the development of synthesis methods that can enable construct Au@ TiO_2 core/yolk-shell nanocomposite with precisely controlled spatial structure is still highly required to meet practical application and reveal mechanism of the plasmon-enhanced photocatalytic function of noble metal-semiconductor core/yolk-shell nano-structures. Excitingly, coaxial electrospinning technology as a flexibility, versatile and continuous fibers production method, shows significant advantages in construction of hollow nanofibers through the individual design of shell and core components [33]. In this case, a mixed polymer solution with metal oxide precursors as shell and paraffin oil as core material is the most commonly method [34]. It is worth noting that the direct addition of HAuCl_4 to paraffin oil is infeasible due to the separation of the inorganic and organic phases, meanwhile it is difficult to controllably generate the Au NPs. If it is possible to prepared the Au NPs highly dispersing in oil phase which could realize the Au NPs inner loaded the TiO_2 HNFs by coaxial electrospinning. But the low lipophilicity of ordinary Au NPs preventing their well dispersion in the paraffin oil. Therefore, it is necessary to modify the surface of Au NPs to amplify their lipophilicity. In alignment with this, advances in stepwise phase transfer techniques have enabled the dispersion of highly lipophilic Au NPs with a paraffin-like organic phase. Unfortunately, related works have seldom reported up to date.

This study demonstrates the successful preparation of TiO_2 hollow nanofibers with large-size mesopores on the shell using coaxial electrospinning and PEI regulation. The uniform and stable dispersion of Au NPs in paraffin oil as the core is achieved through a stepwise phase transfer technique. The resulting composite, with Au NPs loaded on the inner wall of TiO_2 mesopores hollow nanofibers, exhibits significantly improved CO photooxidation rates compared to commercial P25 TiO_2 and ordinary TiO_2 hollow nanofibers. The large mesopores enhance surface area and O_2 adsorption, while the Au NPs trap electrons and catalyze O_2 activation. The study also considers the often-overlooked photothermal effect of Au plasmon resonance on CO photooxidation. This work offers a key method for designing and producing highly active TiO_2 -based mesoporous hollow photocatalytic materials.

2. Experimental section

2.1. Synthesis of materials

In this experiment, all the chemical and reagents were of analytical grade and used without further purification, which were purchased from Aladdin. Deionized water used in all the experiments has a resistivity of 18.2 $\text{M}\Omega\cdot\text{cm}$.

2.1.1. Synthesis of TiO_2 mesoporous hollow nanofibers

The TiO_2 nanoparticles (TO NPs) were prepared by hydrothermal method [35]. The TiO_2 mesoporous hollow nanofibers (TO MPHNFs) were prepared with the coaxial electrospinning. Typically, TBT (tetrabutyl titanate, 99 %, 3 g) and different mass (0, 0.2, 0.4 and 0.6 g) PEI (polyethylenimine, $\text{Mw}\sim 600$, 99 %) were dissolved in ethanol (5 mL), then added PVP (polyvinylpyrrolidone, $\text{Mw}\sim 1300000$, 0.3 g) in the solution for 12 h under stirring obtained the precursor solution. Subsequently, precursor solution and paraffin oil were separately as shell and core solution which were transferred into the coaxial electrospinning apparatus. The coaxial needle consisted of 18# stainless steel needle as the outer one and 25# stainless steel needle as the inner one. The nanofibers were prepared by device for electrospinning (working distance of 20 cm, the operating voltage of 14 kV, temperature about 30 °C, humidity below 20 and the outer and inner injection rate at 0.8 and 0.2 mL h^{-1} , respectively). The nanofibers were dried at 80 °C in the oven overnight, then heated in the muffle furnace at 500 °C for 2 h with heating rate of 1 °C min^{-1} . The obtained TiO_2 mesoporous hollow nanofibers were signed as TO HNFs, 0.2TO MPHNFs, TO MPHNFs and 0.6TO MPHNFs, respectively.

2.1.2. Synthesis of Au@ TiO_2 mesoporous hollow nanofibers

The synthetic method used for oil-soluble Au NPs involves a two-phase liquid-liquid system [36,37]. Typically, the Au NPs washed by ethanol to remove toluene and excess thiol. Then, the Au NPs were extracted from ethanol into n-hexane by phase transfer. The Au NPs dispersion was miscible with a certain amount of paraffin oil and removed n-hexane using rotary evaporator for preparation paraffin oil dispersion. The paraffin oil with dispersion oil-soluble Au NPs replaced pure paraffin oil as core solution for electrospinning and calcining as same with TO MPHNFs. The samples were signed as xAu@TO MPHNFs ($x = 0.5, 1, 1.5$ and 2), where x represents the mass ratio (0.5, 1, 1.5 and 2 %) of Au NPs to TiO_2 . It is noteworthy that there is no loss of Ti or Au during the electrospinning process, that the actual contents of Ti and Au align with the ingredient proportions in various samples.

2.2. Materials characterization

The X-ray diffraction (XRD) was used with a $\text{Cu K}\alpha$ radiation and recorded the patterns on a Bruker D8 advance. The N_2 adsorption-desorption test were determined by of Quanta Chrome Autosorb iQ. Scanning electron microscope (SEM) images were using ZEISS-sigma 500 instrument at 5 kV voltage. Transmission electron microscopy (TEM) images were using JEOL JEM-F200 electron microscope at 200 kV voltage. The X-ray photoelectron spectra (XPS) were recorded on Kratos-AXIS ULTRA DLD instrument equipped. The UV-vis diffuse reflectance spectrum (DRS) curve was used Shimadzu UV-2700 spectrophotometer and BaSO_4 as basic carrier. The surface photovoltage spectroscopy (SPS) were surveyed with a self-built apparatus under the different gas atmospheres, equipped with a lock-in amplifier (SR830, USA) synchronized with a light chopper (SR540, USA). The O_2 -temperature-programmed desorption (O_2 -TPD) were using Tianjin XQ TP5080 auto-adsorption apparatus with a thermal conductivity detector (TCD). The electron paramagnetic resonance (EPR) tests of free radicals were carried out on the Bruker EMX plus model spectrometer.

2.3. In-situ Fourier transform infrared spectra

The *in-situ* Fourier transform infrared spectra (*in-situ* FT-IR) was performed with a Nicolet iS50 FTIR spectrometer to record the working curve. The experimental settings were as follows: the MCT detector was chosen with the resolution of 4 cm^{-1} and scans 16 for the samples, the examination range is 1000 cm^{-1} to 4000 cm^{-1} . The samples mixed with KBr were compressed and placed in a custom-fabricated IR reaction chamber which sealed with ZnSe windows. Initially, the samples were purged with N_2 (the flow rate at $40\text{ mL}\cdot\text{min}^{-1}$) at $170\text{ }^\circ\text{C}$ for 2 h to eliminate any impurity gas adsorbed on the surface. After cooling down to $25\text{ }^\circ\text{C}$, the spectra of the samples were collected as a background reference. Then, high purity O_2 was introduced into the reaction chamber at a flow rate of $40\text{ mL}\cdot\text{min}^{-1}$ for 30 min. Afterwards, 5 vol% CO balanced with high purity O_2 as the probe gas was introduced into the system at a total flow rate of $40\text{ mL}\cdot\text{min}^{-1}$ for 1 min and balanced for 30 min in sealed reaction chamber, the data were continuous collected. The reaction chamber could switch light source and regulate temperature. Subsequently, the FT-IR spectra were collected at different irradiation and temperature intervals to investigate the produced intermediates.

2.4. Evaluation of photocatalytic activity

The photocatalytic activities of the samples were evaluated by analyzing the photocatalytic oxidation rates of CO. To evaluate the recyclability and stability of the photocatalyst, the catalyst was sequentially washed with deionized water and ethanol, then dried at $80\text{ }^\circ\text{C}$ to remove all absorbed reactants and products between each run. The reaction was carried out in a 600 mL reactor equipped with thermostatic water. After filling the reaction vessel with O_2 and subsequently injecting CO (0.6 mL), the CO concentration in the reactor was 1000 ppm. The CO concentration was detected using a GC2002 gas chromatograph (GC) with FID detector. After the gas was diffused for 30 min, 0.5 mL of gas was introduced into the injector and injected into the GC to measure the peak area of CO (S0). The peak area of the remaining CO (St) in the reactor was measured after irradiation for 1 h using 300 W Xenon arc lamp and the light intensity is estimated to be 400 mW cm^{-2} . Given a specific concentration range, the peak area of CO was directly proportional to the actual content, so the formula was used to calculate the photocatalytic CO oxidation activities of resulting samples.

2.5. Evaluation of thermal-assist photocatalytic activity

Evaluation of thermal-assist photocatalytic activity was similar to the photocatalytic. The thermal-assist photocatalytic activity was obtained according to the above procedures except for using corresponding light irradiation and heat. In order to simulate thermal-assist photocatalysis, the circulating water with different temperatures was used into the reactor to achieve thermal assistance. The surface temperature

of catalyst was measured by infrared temperature sensor to realize non-contact temperature measurement.

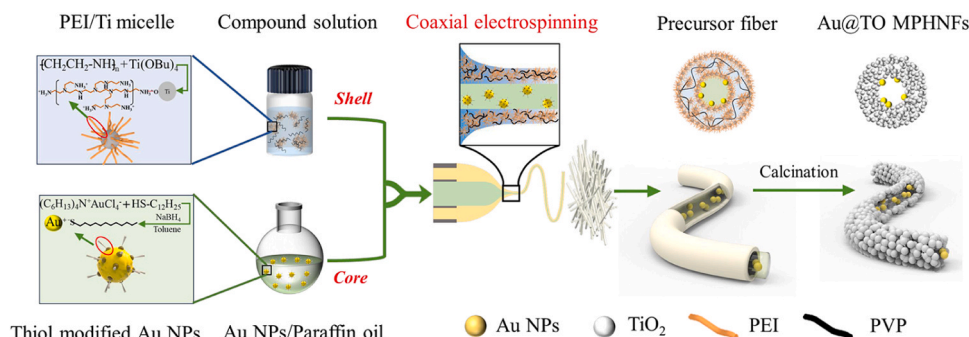
The other detailed experimental description is provided in Appendix A. [Supplementary data](#).

3. Results and discussion

3.1. Synthesis schematic and structural characterization

The design and synthetic pathway of the Au@TO MPHNFs is illustrated in [Scheme 1](#). The large number of amino groups in PEI can interact with metal alkoxides to form micelles through hydrogen-bond, once TBT is mixed with PEI. Then, it disperses into ethanol and PVP is added to increase the viscosity of the solution and act as shell precursor. On the other hand, the thiol modified Au NPs have been synthesized in toluene using the reported method, and the Au NPs are washed and dispersed by ethanol. Subsequently, so as to ensure well dispersion of Au NPs, the extraction of Au NPs from ethanol is facilitated by employing n-hexane as a phase transfer solvent. And incorporate it into paraffin oil with miscibility to exchange the Au NPs due to the relatively low boiling of n-hexane, it can be easily eliminated through rotary evaporation. The paraffin oil with dispersed Au NPs can serve as uniform core precursor. The Au@TiO₂ precursor fibers are achieved through the coaxial electrospinning technique using Au NPs dispersed paraffin oil as the core and PEI regulated TiO₂ sol-gel/polymer solution as the shell. Concurrently, the Au NPs are tightly attached to the inner wall of the hollow fibers. Subsequent calcination removes the organic molecules from the nanofibers surface, resulting in Au@TO MPHNFs. For comparison, pure paraffin oil, instead of Au-paraffin oil has been used to prepare TO MPHNFs by the identical coaxial electrospinning process.

To explore the influence of PEI porogen on nanofibers, nanofibers with varied content of PEI (addition is 0, 0.2, 0.4 and 0.6 g which are signed as TO HNFs, 0.2TO, TO and 0.6TO MPHNFs, respectively) have been synthesized, and TiO₂ NPs (TO NPs) has been also compared. The [Fig. S1 and S2](#) show that the TO NPs are typical anatase TiO₂. It is obvious that TO HNFs are better than TO NPs in specific surface areas ([Fig. S3](#)) and charge separation ([Fig. S4](#)) for a great CO oxidation activity ([Fig. S5](#)). Obviously, HNFs structures have significant advantages over nanoparticles. As shown in [Fig. 1a and S6](#), the X-ray diffraction (XRD) patterns of TO HNFs observe phase-mixed of TiO₂ that consists of anatase (JCPDS no. 89-4921) and rutile (JCPDS no. 21-1276) nanocrystals [38]. In contrast, PEI introduced samples match to anatase TiO₂ which indicate that PEI could inhibit the phase transformation after high temperature treatment as we expected. With the increase of PEI content, the specific surface area of the nanofibers increases ([Fig. S7](#)), meanwhile the charge separation and subsequent CO oxidation performance are increased first and then decreased, and reaching the highest value at 0.4 ([Fig. S8-S10](#)). Therefore, the 0.4TO MPHNFs are selected as the test sample and labeled as TO MPHNFs for subsequent experiments. Scanning electron microscope (SEM) images ([Fig. 1b and c](#)) exhibit that TO MPHNFs have a relatively uniform hollow structure with an average



Scheme 1. Schematic synthetic pathway and mechanism of Au@TO MPHNFs.

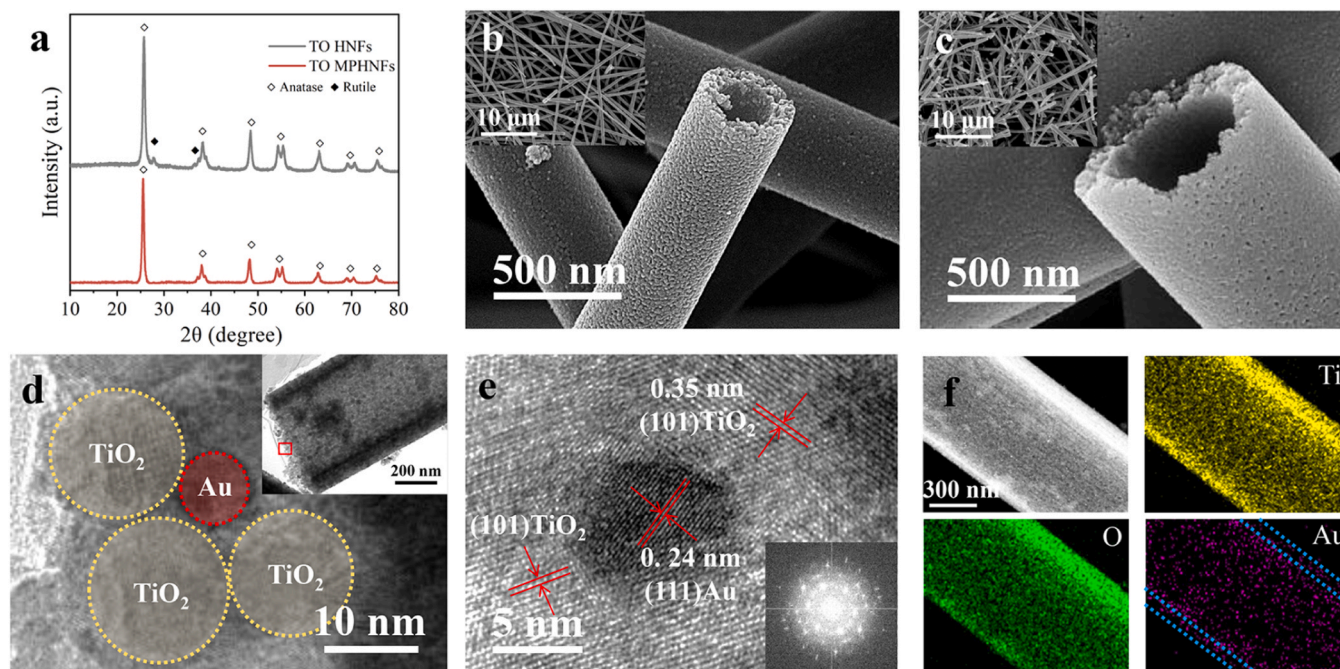


Fig. 1. XRD patterns(a) and SEM images (b and c) of TO HNFs and TO MPHNFs, respectively. TEM, HRTEM and EDS elemental mapping images (d-f) of the Au@TO MPHNFs. The areas highlighted in red and yellow represent Au and TiO₂ nanoparticle, respectively.

diameter of about 600 nm and wall thickness of around 100 nm, larger than those of TO HNFs. The high-resolution transmission electron microscopy (HRTEM) image (Fig. S11) of TO MPHNFs reveals the fibrous skeleton is composed of numerous nanoparticles with a diameter about of 15 nm and aggregated along the fibers. Conspicuous lattice fringes with ad-spacing of 0.35 nm can be found in the HRTEM image, corresponding to the (101) plane of anatase [17].

Meanwhile, in order to further explore the role of PEI on nanofibers, the reference samples porous hollow nanofibers are prepared by P123 and F127 as porogens, which are signed as P123-TO MPHNFs and F127-TO MPHNFs, respectively. The Fig. S12 is the XRD patterns of the P123-TO and F127-TO MPHNFs which are treated by 500 °C calcination. It is noteworthy that the diffraction peaks referring to the rutile TiO₂ appear in P123-TO and F127-TO MPHNFs like TO HNFs, indicating that the two samples undergo phase transformation at high temperature. It is deduced that the P123 and F127 have little stabilizing effect on TiO₂ crystals. In addition, although P123-TO and F127-TO MPHNFs have a larger specific surface area, their excessively small pores (3 nm) limit the mass transfer process (Fig. S13) [11]. In contrast, the mesoporous around 14 nm of TO MPHNFs can be maintained by PEI as pore protectors. Consequently, TO MPHNFs exhibit the best photocatalytic CO oxidation performance (Fig. S14). The above data indicate that PEI prevents TiO₂ phase transformation during calcination, and thus maintain a complete mesoporous structure.

The content of the cocatalyst influence the catalytic performance significantly, thus, TO MPHNFs with different content of Au (xAu@TO MPHNFs, x = 0.5, 1, 1.5 and 2) have been synthesized. The prefabricated Au NPs is monodispersed and relatively uniform with an average diameter of about 5 nm (Fig. S15). It is clearly showed from TEM and SEM images (Fig. 1d and S16) of Au@TO MPHNFs, the Au NPs are integrated on TO MPHNFs successfully. One can clearly see that the Au NPs are uniformly distributed within the nanofibers and are constant in size (Fig. 1e). Moreover, the energy dispersive X-ray (EDX) elemental mapping images (Fig. 1f) exhibit predominant Au element distribution within the inner wall of the nanofibers. The crystal structure, specific surface area and pore size distribution curve of all samples have been observed by XRD and N₂ adsorption-desorption test (Fig. S17 and S18). It is to be expected that the introduction of Au NPs did not affect the

crystal structure, specific surface area and pore size of the nanofibers during electrospinning. Owing to the strong absorption of Au into visible light, the absorption of the samples in the vision region is gradually heightened as the Au content increase (Fig. S19). Unexpectedly, the photocatalytic CO oxidation performance of the samples are increased initially and then decreased with the increasing of Au content, peaking at 1.5 (Fig. S20). It is may attributed to excessive Au NPs occupying the exposed catalytic sites on TiO₂ and simultaneously impeding light absorption. As a result, the 1.5Au@TO MPHNFs are selected as the test sample and labeled as Au@TO MPHNFs. To provide a comparative analysis, TO MPHNFs with Au NPs loaded outer have also been prepared. Evidently, the visible light absorption and the photocatalytic CO oxidation performance of Au@TO MPHNFs are far superior to the outer loaded Au (Fig S21 and S22), which may be due to the noble metal NPs situated in TiO₂ HNF promote visible light absorption via reflection within the hollow nanofibers [30].

To further demonstrate the effective combination of Au and TiO₂, the PTO and Au@TO MPHNFs are investigated by X-ray photoelectron spectrum (XPS) measurements (Fig. S23). The two peaks centered at 84.0 eV and 87.6 eV correspond to Au 4f_{7/2} and 4f_{5/2}, respectively (Fig. S24). A slight blue shift has been noted in the high-resolution Ti 2p and O 1s (Fig. 2a and S25) binding energies of Au@TO MPHNFs when compared to the TO MPHNFs, which attribute to electron transfer from TiO₂ to Au on the Au/TiO₂ interface, that lead the outer electron cloud density of Ti and O in the composite is reduced. Combined with TEM, it clarifies that Au NPs display close interfacial contact on the inner wall of the TO MPHNFs, achieve by the one-step coaxial electrospinning technique. The UV-vis diffused reflectance spectra (DRS) of the samples are shown in Fig. 2b, compared with the TO HNFs, the absorption of TO MPHNFs at 400 nm to 500 nm can be ascribed to the N-doping or surface defects by PEI induced, while the wide visible region absorption of Au@TO MPHNFs is attributed to SPR effect of Au. Moreover, the N₂ adsorption-desorption measurements (Fig. 2c) show that TO HNFs are the typical characteristics of type IV with H3 hysteresis loop, which proves that the TO HNFs possess mesoporous structures through disordered accumulation of particles. With the introduction of PEI, it is found that the TO MPHNFs exhibit a H2 hysteresis loop along with another typical pore condensation step at a higher relative pressure (P/P₀ = 0.5 –

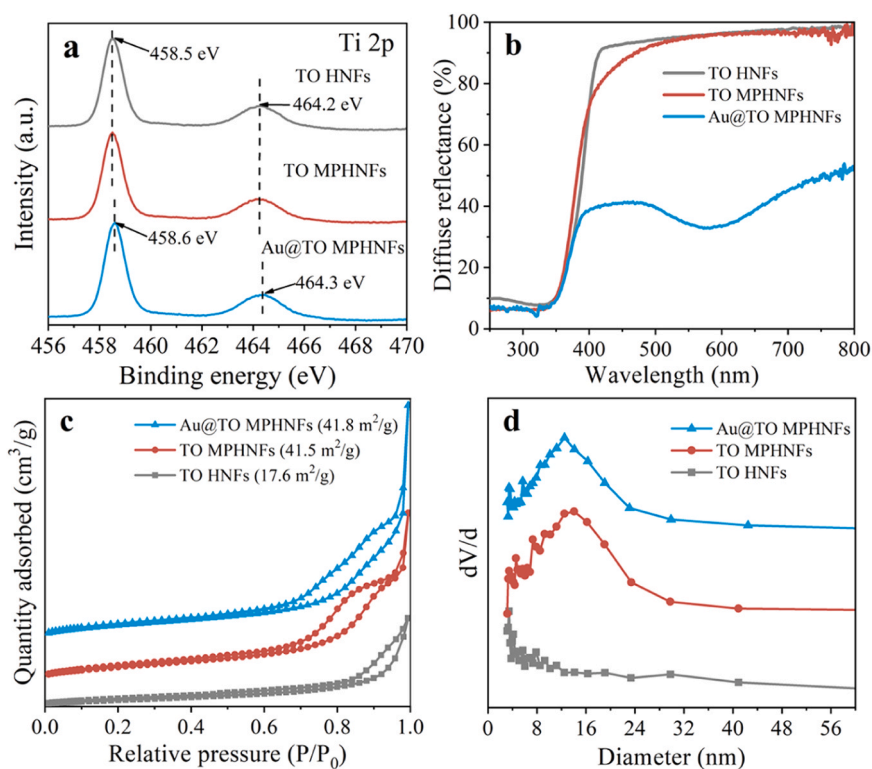


Fig. 2. Ti 2p XPS high-resolution spectra (a), UV-vis diffuse reflectance spectrum (b), N₂ adsorption-desorption isotherm curves (c) and pore size distributions (d) of TO HNFs, TO MPHNFs and Au@TO MPHNFs.

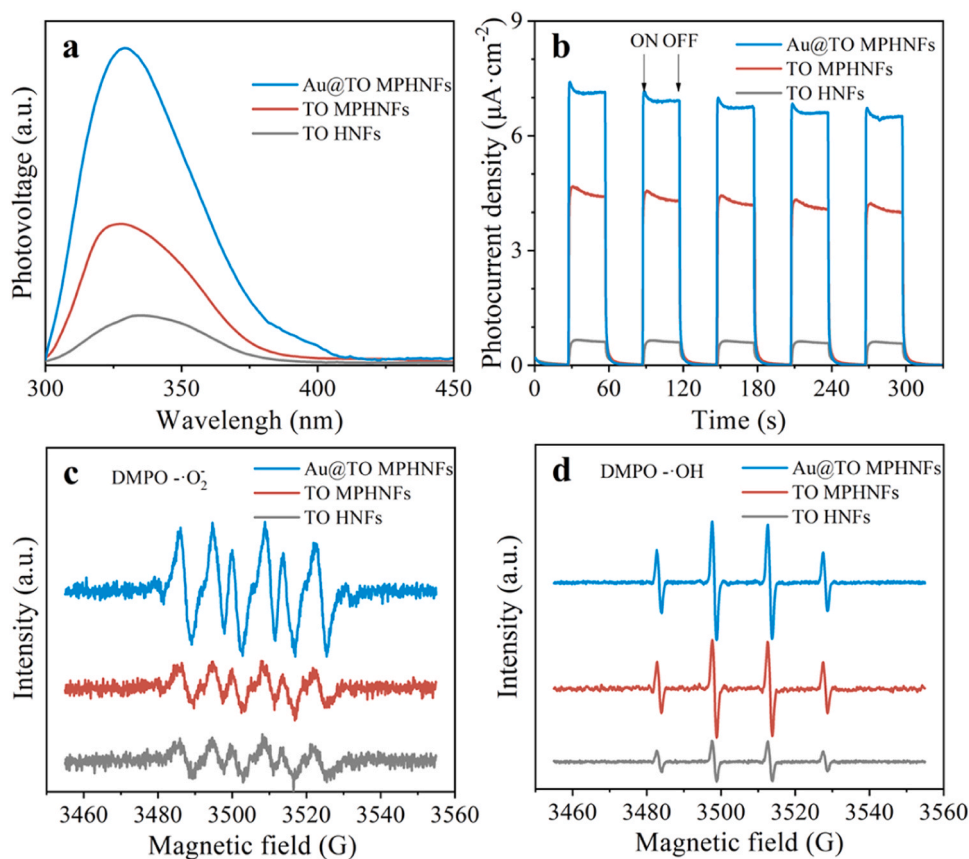


Fig. 3. SPS responses (a), photocurrent response density measurement (b), EPR spectra of the DMPO-·O₂ in methanol (c) and the DMPO-·OH adducts in water (d) of TO HNFs, TO MPHNFs and Au@TO MPHNFs.

0.9). This suggests the presence of a significant number of columnar mesopores on each single fibers [39]. The specific surface areas of the TO MPHNFs ($41.5 \text{ m}^2 \text{ g}^{-1}$) and Au@TO MPHNFs ($41.8 \text{ m}^2 \text{ g}^{-1}$) exceed that of the TO HNFs ($17.6 \text{ m}^2 \text{ g}^{-1}$). The Fig. 2d demonstrates that the appropriate Au NPs are demonstrated no apparent effect on the porous structure upon loading into the TO MPHNFs (approximately 14 nm). Combined with the above results, the preparation of TiO_2 MPHNFs with inner loaded Au NPs, achieved via appropriate PEI controlled coaxial electrospinning.

3.2. Charge separation and photoactivity

Based on the structural advantage of the aforementioned mesoporous nanofibers, we further explore the charge separation of catalyst. It is an effective method to study the photogenerated charge separation by the intensity of the surface photovoltage spectroscopy (SPS) response, photocurrent response density measurement and electrochemical impedance spectra. As displayed in Fig. 3a, the SPS response intensity of Au@TO MPHNFs is significantly heightened compared to that of TO MPHNFs and TO HNFs. This suggests an effective improvement in charge separation fostered by both the specific MPHNFs structure and loaded Au NPs, benefiting to O_2 capture photogenerated electron. Photocurrent response density measurement and electrochemical impedance spectra analyses (Fig. 3b and S26) are further corroborating the result, both of which align well with the SPS responses. To validate the separation and transfer of photogenerated charges, the EPR measurement is conducted to discriminate the produced active species by samples under irradiation with 5,5-dimethylpyrrolidine-N-oxide (DMPO) using as the spin-trapping agent [40]. The DMPO- O_2^\cdot EPR (Fig. 3c) signal detected confirms the occurrence of a reduction reaction between photogenerated electrons and adsorbed O_2 ,

resulting in the production of an active species $\cdot\text{O}_2^\cdot$. Compared with TO HNFs and TO MPHNFs, the Au@TO MPHNFs show the most significant signal enhancement, pointing towards the effective promotion of charge separation via the reaction of photogenerated electrons with O_2 . Simultaneously, the generation of DMPO- $\cdot\text{OH}$ EPR (Fig. 3d) signal, displaying an intensity ratio of 1:2:2:1, identifies the production of $\cdot\text{OH}$ through the oxidation of photogenerated holes with H_2O . The TO MPHNFs signal gain more intensity than the TO HNFs, indicating the charge separation facilitated by photogenerated holes to oxidize H_2O into $\cdot\text{OH}$. Furthermore, the electron transfer facilitated by Au NPs as electron trap will additionally enhance the oxidation of the holes, resulting in the Au@TO MPHNFs exhibiting the highest signal. Clear evidence is thus provided to demonstrate that both the regulation of PEI and the introduction of Au NPs promote prominent positive effects on the charge separation of TO MPHNFs, highlighting the crucial roles of mesoporous nanofibers structure and O_2 activation.

The activation of O_2 , a critical initial step in CO oxidation, requires the consumption of photogenerated electrons which concurrently promotes the oxidation reaction of hole within photocatalysis. To explore the promotion of O_2 adsorption on the charge separation, the SPS responses under varying atmosphere (Fig. 4a) are tested. It is observable that TO MPHNFs without photovoltaic response signal in N_2 but the Au@TO MPHNFs show a low photovoltaic response signal within the same environment, which is ascribed to Au NPs trapped photogenerated electrons in N_2 . As expected, when the experiments have been sequentially switched to air and O_2 atmospheres, the samples show an elevated photovoltaic response signal due to the increased O_2 content. It is confirmed that O_2 could play a positive role in the charge separation process. For further exploring the direct relationship between the adsorption capacity of O_2 with the photocatalytic activity of the samples, the O_2 -TPD has been tested (Fig. 4b). The samples display two

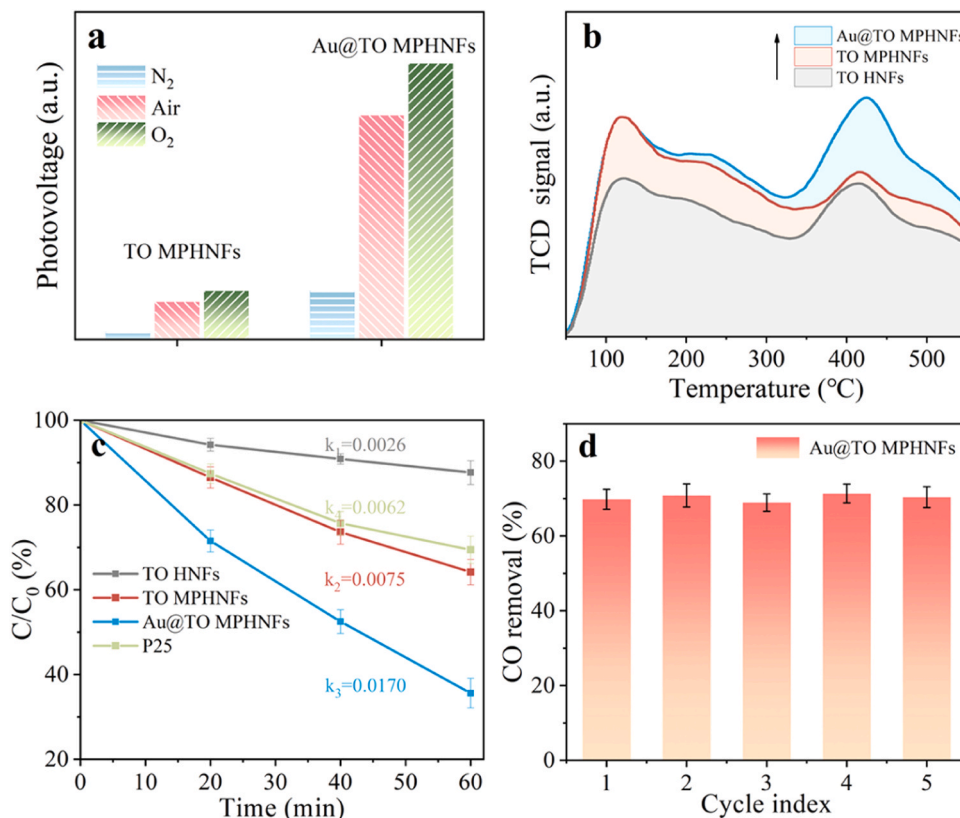


Fig. 4. Intensities of SPS response peaks at 350 nm in different atmospheres (a), temperature-programmed desorption curves for O_2 (b) of TO HNFs, TO MPHNFs and Au@TO MPHNFs. The photoactivity for CO oxidation of TO HNFs, commercial TiO_2 P25, TO MPHNFs and Au@TO MPHNFs (c). The photoactivity for CO oxidation of Au@TO MPHNFs over 5 irradiation cycles (d), the data are presented as the mean \pm standard ($n = 3$).

peaks in the temperature range of 50–300 °C and 350–500 °C, which are assigned to desorption of physically absorbed O₂ and chemisorbed O₂, respectively [41]. It is evident that the specific MPHNFs structure promotes physically absorbed O₂, while the introduction of Au NPs accelerates chemisorbed O₂, leading to robust O₂ activation.

According to the above analysis, it is speculated that the Au@TO MPHNFs has an exceptional photocatalytic CO oxidation performance. When matched against TO MPHNFs and TO HNFs, the CO oxidation conversion of the Au@TO MPHNFs is significantly elevated, which is consistent with the result of charge separation analysis. The Au@TO MPHNFs exhibit a major improvement in photocatalytic CO oxidation performance with enhancements approximately 2.3, 2.7 and 7.4-fold greater than TO MPHNFs, commercial P25 and TO HNFs, respectively (Fig. 4c). Both Au@TO MPHNFs and TO MPHNFs possess porous and hollow structure, with the nanofibers constructing a loose 3D network that facilitates the mass diffusion for gaseous reaction. Furthermore, the efficacy of Au NPs in promoting charge separation and providing more catalytic site for O₂ activation also contributed to the improvement in photoactivity. In addition, the photocatalytic performance of Au@TO MPHNFs displays no obvious decline after 5 cycles (Fig. 4d), which indicates their fine stability.

3.3. Mechanism discussion

In theory, the strong SPR effect of Au under visible light irradiation could generate photoexcited hot carriers to participate in catalytic reactions and also has strong photothermal conversion ability for raising the reaction temperature [42]. Unfortunately, the photothermal effect is overlooked frequently in previous reports. It is imperative to understand photothermal influence on the photocatalytic performance of the catalyst, therefore, the surface temperature of catalyst (Fig. 5a) is tested under different light irradiation. The surface temperature of catalyst raises rapidly and stabilizes within about 20 min. Under UV irradiation,

both TO MPHNFs and Au@TO MPHNFs maintain an average temperature of 32 °C. With the visible light addition, the temperature of Au@TO MPHNFs raise to about 75 °C but TO MPHNFs remain at about 40 °C. It explains that the substantial photothermal conversion is derived from excited Au NPs triggering SPR effect under visible light. In order to further confirm the influence of the thermal effect on catalysis, the photocatalysis tests have been conducted under different light irradiations with extra thermal assistance. The Fig. 5b presents the CO conversion rate of TO MPHNFs and Au@TO MPHNFs under different light irradiation and with thermal assistance at 75 °C (the power densities of UV+vis, vis and UV are measured as 400, 335 and 65 mW·cm⁻², respectively). The samples exhibit superior CO oxidation performance under UV illumination due to the excitation of TiO₂. Further exploration shows that the separate thermal addition and SPR effect excited by visible light accounted for less contributions to CO oxidation. However, incorporating UV irradiation and thermal-assistance boost the performance of the samples, may attribute to the heat that accelerated the mass transfer and promoted the O₂ activation [43]. When illumination altered to the UV+vis, the photocatalytic activity of Au@TO MPHNFs exhibits a significantly improvement that is attributed to the photo-photothermal synergies driven by the SPR effect of Au. In contrast, the photocatalytic activity of TO MPHNFs remained relatively unchanged under both the UV and UV+vis irradiation, revealing its inability for photothermal conversion. Based on the above analysis, it is concluded that the introduction of Au serves dual purposes-as a co-catalyst and a heat source-elevating the reaction temperature around the catalysis site to coordinate photocatalytic CO oxidation.

Shedding light on the entire photocatalytic reaction mechanism with a focus on the catalytic oxidation process, we have studied the adsorption of reactants on typical samples using *in-situ* FT-IR (Fig. 5 c-f). The peaks at 2117 and 2173 cm⁻¹ are assigned to the stretching vibration of the CO molecules adsorbed onto the surface of samples [44]. Concurrently, it is observed a rapid production of reaction intermediates under

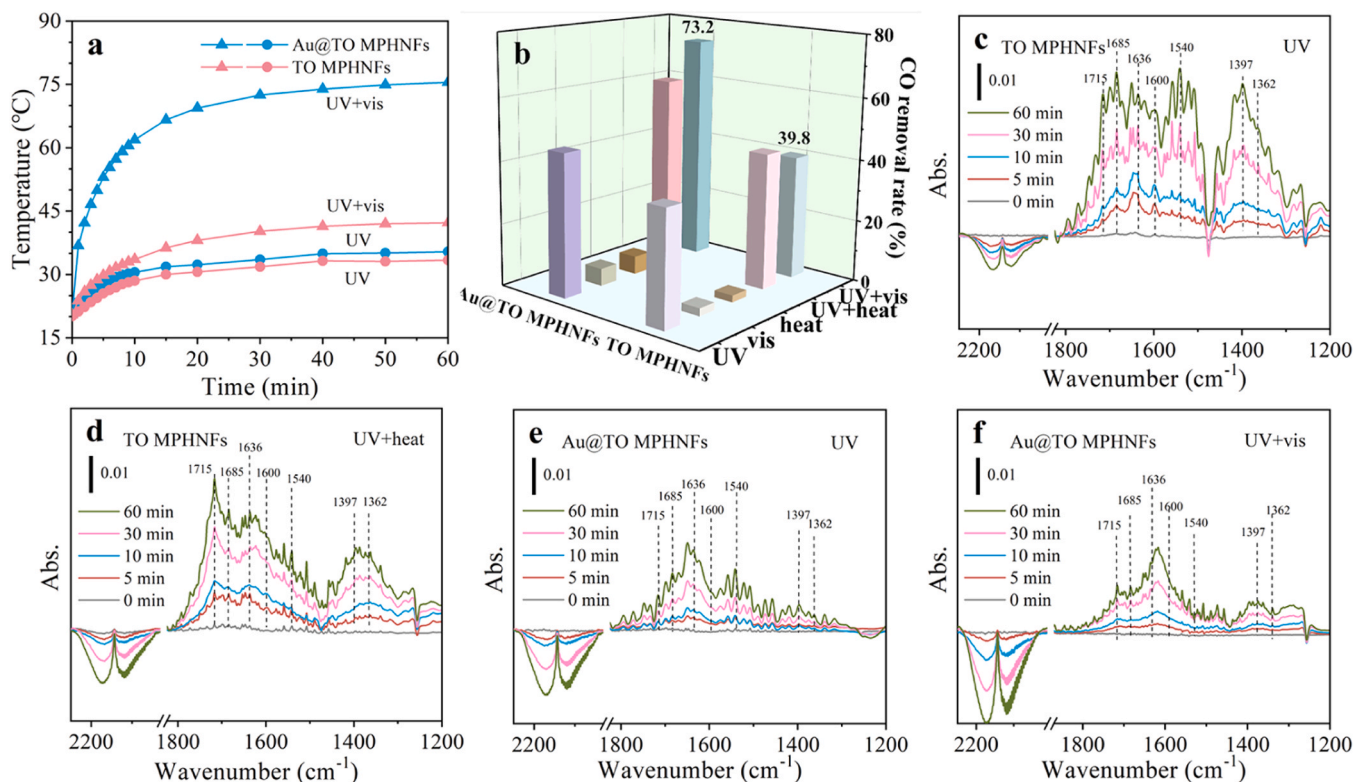


Fig. 5. Temperature elevation of catalyst surface under UV or UV+vis irradiation as a function of irradiation duration (a), Photoactivity for CO oxidation under different conditions of TO MPHNFs and Au@TO MPHNFs (b), and *in-situ* FT-IR spectra with varying irradiation and temperature for different time on TO MPHNFs (c and d) and Au@TO MPHNFs (e and f).

light illumination, the peaks at 1685 and 1540 cm^{-1} likely correspond to the COOH^* intermediate (CO reacting with surface activated hydroxyls) [45,46]. This COOH^* has quickly transformed to bicarbonates (HCO_3^-) and carbonate (CO_3^{2-}) in presence of reactive oxygen species, for which observe the HCO_3^- at 1715 cm^{-1} and 1397 cm^{-1} , and the CO_3^{2-} at 1600 and 1362 cm^{-1} , respectively [47]. Finally, the HCO_3^- and CO_3^{2-} on the catalyst surface is decomposed to form CO_2 . In addition, the peak located at 1636 cm^{-1} may be originated from the bending vibration of the chemisorbed water on the TiO_2 surface (δHOH) [48].

The conversion rate of the intermediate species is the rate limiting step of the CO oxidation process. To investigate the role of thermal enhancement in this step, TO MPHNFs is tested under UV and UV+heat (added 75 $^\circ\text{C}$). When external heat has been added to UV irradiation, the peaks exhibit a significant attenuation (Fig. 5c and d), indicating the thermal effect can promote COOH^* intermediate conversion leading to CO consumption and thus improve photocatalytic activity. With incorporating Au NPs, it is shown the intermediate species of COOH^* as well as $\text{CO}_3^{2-}/\text{HCO}_3^-$ had less accumulation and more CO consumption under the UV (Fig. 5e), which explain Au can promoting the conversion of intermediate species and accelerating the desorption of reaction products. Upon supplementing thermal conditions, we have observed a decrease in accumulation of intermediate and an increase in consumption of CO (Fig. S27), indicating that the thermal effect is conducive to inhibit the accumulation of intermediate for accelerating the consumption of CO. Finally, the substitution of thermal condition with visible light irradiation leading to an even more pronounced influence (Fig. 5f), suggesting that the thermal effect has further enhanced under visible light irradiation. Findings demonstrate that photothermal conversion contributed by SPR effect of Au under visible light irradiation expedite the conversion of intermediate species and desorption of reaction products, resulting in faster CO consumption and hence, enhancing photocatalytic activation of CO oxidation.

Base on the aforementioned results and analysis, a possible reaction mechanism of CO oxidation over Au@TO MPHNFs under UV-vis irradiation is proposed in Fig. 6. Au@TO MPHNFs has the hollow porous structure which is conducive to mass transfer and light absorption. In fact, CO mainly adsorbs on TiO_2 , and the intervention of Au NPs promote chemisorbed O_2 . When the Au@TO MPHNFs are irradiated by full light, the excited electron-hole pairs would be generated on the surface of the TiO_2 under UV irradiation and the excited Au NPs liberate the thermal energy of SPR effect under visible light irradiation. Subsequently, the photogenerated electrons have been transferred to Au NPs through the interface of Au and TiO_2 . The presence of Au as a co-catalysis efficiently activates O_2 with thermal effect while simultaneously promoting the holes activate adsorbed CO and hydroxyl group to form intermediate COOH^* on TiO_2 . The intermediate further undergoes a reaction with the active oxygen species to generate HCO_3^- . The intermediate species of HCO_3^- may also be transformed into CO_3^{2-} deposited on the TiO_2 surface or the Au/ TiO_2 interface. Consequently, the HCO_3^- and CO_3^{2-} intermediate species could quickly decompose into CO_2 with the thermal effect of Au NPs which provide adequate energy for intermediates decomposition and CO_2 desorption, which provide catalytic sites for the subsequent oxidation reaction.

4. Conclusions

In summary, TiO_2 mesoporous hollow nanofibers (TO MPHNFs) with inner loaded Au NPs have been successfully synthesized via one-step coaxial electrospinning process, and shows excellent photocatalytic CO oxidation performance. For the materials construction, the PEI as a porogen is the key to achieving controllable preparation of large mesoporous structures on the wall of TiO_2 nanofibers with highly thermally stable. As well as the uniform dispersion of prefabricated Au NPs in paraffin oil is successfully achieved through the phase transfer process, which is a prerequisite for the controlled inner loading of Au NPs in the TO MPHNFs by the coaxial electrospinning process. The high

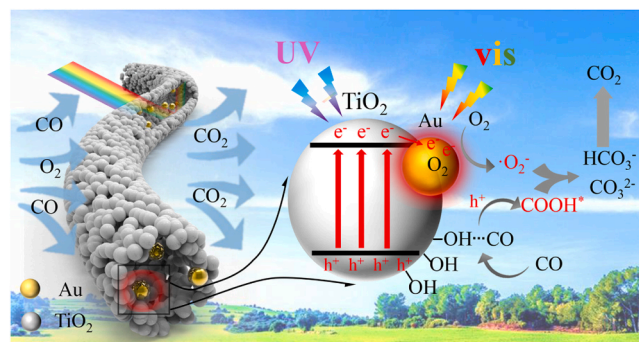


Fig. 6. Schematic illustration of photogenerated charge transfer and the CO oxidation process on Au@TO MPHNFs.

photocatalytic activity is primarily attributed to the mesoporous hollow nanofibers structure with boosted mass transfer process of gas-phase reactants, elevated the specific surface, exposed active sites, and enhanced the utilization of visible light by the inner loaded Au NPs. Furthermore, the impact of Au NPs on photogenerated charge separation, O_2 activation, and the photothermal effect on the photocatalytic reaction has been further elucidated. This study provides an essential strategy and reference for expanding the application of coaxial electrospinning technology in constructing heterojunction photocatalytic materials with core-shell mesoporous hollow nanofibers structure. Additionally, it sheds light on the mechanism of the thermal effect of SPR metal on photocatalytic performance.

CRediT authorship contribution statement

Tianwei Dou: Writing – original draft, Visualization, Validation, Investigation, Data curation. **Lei Sun:** Writing – review & editing, Methodology, Formal analysis. **Zhijun Li:** Writing – review & editing, Formal analysis. **Yangyang Zhu:** Investigation. **Zhanyu Chu:** Investigation. **Liqiang Jing:** Writing – review & editing, Supervision, Funding acquisition, Conceptualization.

Declaration of Competing Interest

The authors declare that they have no known competing financial interests or personal relationships that could have appeared to influence the work reported in this paper.

Data availability

Data will be made available on request.

Acknowledgments

The authors are grateful for financial support from the NSFC project (U2102211, 21905080, U23A205760), Heilongjiang Province Youth Innovation Talent Development Program for Ordinary Institutions of Higher Education (UNPYSCT-2020003), Heilongjiang Province Postdoctoral Science Foundation project (LBH-Z19094), China Postdoctoral Science Foundation project (2021M701126) and Basic Research Fund of Hei-longjiang University in Heilongjiang Province (2021-KYYWF-0038).

Appendix A. Supporting information

Supplementary data associated with this article can be found in the online version at doi:10.1016/j.apcatb.2024.124112.

References

- [1] J.J. Rose, L. Wang, Q. Xu, C.F. McTiernan, S. Shiva, J. Tejero, M.T. Gladwin, Carbon monoxide poisoning: pathogenesis, management, and future directions of therapy, *Am. J. Respir. Crit. Care Med.* 195 (2017) 596–606, <https://doi.org/10.1164/rccm.201606-1275CI>.
- [2] S. Mahajan, S. Jagtap, Metal-oxide semiconductors for carbon monoxide (CO) gas sensing: a review, *Appl. Mater. Today* 18 (2020) 100483, <https://doi.org/10.1016/j.apmt.2019.100483>.
- [3] Y. Li, S. Wu, J. Wu, Q. Hu, C. Zhou, Photocatalysis for efficient abatement of CO and VOCs, *J. Mater. Chem. A* 8 (2020) 8171–8194, <https://doi.org/10.1039/d0ta00029a>.
- [4] X. Ma, J. Albertsma, D. Gabriels, R. Horst, S. Polat, C. Snoeks, F. Kapteijn, H. B. Eral, D.A. Vermaas, B. Mei, S. de Beer, M.A. van der Veen, Carbon monoxide separation: past, present and future, *Chem. Soc. Rev.* 52 (2023) 3741–3777, <https://doi.org/10.1039/d3cs00147d>.
- [5] M.L. Ovcharov, V.M. Granchak, Photocatalytic activation of carbon monoxide on semiconductors and derived nanocomposites: basic principles and mechanisms: a review, *Theor. Exp. Chem.* 55 (2019) 173–200, <https://doi.org/10.1007/s11237-019-09608-3>.
- [6] X. Wu, J. Lang, Z. Sun, F. Jin, Y. Hu, Photocatalytic conversion of carbon monoxide: from pollutant removal to fuel production, *Appl. Catal. B: Environ.* 295 (2021) 120312, <https://doi.org/10.1016/j.apcatb.2021.120312>.
- [7] K. Eid, A. Gamal, A.M. Abdullah, Graphitic carbon nitride-based nanostructures as emergent catalysts for carbon monoxide (CO) oxidation, *Green Chem.* 25 (2023) 1276–1310, <https://doi.org/10.1039/d2gc02748h>.
- [8] X. Ruan, S. Li, C. Huang, W. Zheng, X. Cui, S.K. Ravi, Catalyzing artificial photosynthesis with TiO₂ heterostructures and hybrids: emerging trends in a classical yet contemporary photocatalyst, *Adv. Mater.* (2023) e2305285, <https://doi.org/10.1002/adma.202305285>.
- [9] J.A. Rengifo-Herrera, C. Pulgarin, Why five decades of massive research on heterogeneous photocatalysis, especially on TiO₂, has not yet driven to water disinfection and detoxification applications? Critical review of drawbacks and challenges, *Chem. Eng. J.* 477 (2023) 146875, <https://doi.org/10.1016/j.cej.2023.146875>.
- [10] A. Shoneye, J. Sen Chang, M.N. Chong, J. Tang, Recent progress in photocatalytic degradation of chlorinated phenols and reduction of heavy metal ions in water by TiO₂-based catalysts, *Int. Mater. Rev.* 67 (2021) 47–64, <https://doi.org/10.1080/09506608.2021.1891368>.
- [11] Y. Li, Z. Ren, M. Gu, Y. Duan, W. Zhang, K. Lv, Synergistic effect of interstitial c doping and oxygen vacancies on the photoreactivity of TiO₂ nanofibers towards CO₂ reduction, *Appl. Catal. B: Environ.* 317 (2022) 121773, <https://doi.org/10.1016/j.apcatb.2022.121773>.
- [12] Q. Qiu, L. Xu, D. Wang, Y. Lin, T. Xie, Study on dynamic properties of the photoexcited charge carriers at anatase TiO₂ nanowires/fluorine doped tin oxide interface, *J. Colloid Interface Sci.* 501 (2017) 273–281, <https://doi.org/10.1016/j.jcis.2017.04.075>.
- [13] F. Matter, M. Niederberger, The importance of the macroscopic geometry in gas-phase photocatalysis, *Adv. Sci.* 9 (2022) 2105363, <https://doi.org/10.1002/advs.202105363>.
- [14] M. Ge, Q. Li, C. Cao, J. Huang, S. Li, S. Zhang, Z. Chen, K. Zhang, S.S. Al-Deyab, Y. Lai, One-dimensional TiO₂ nanotube photocatalysts for solar water splitting, *Adv. Sci.* 4 (2017) 1600152, <https://doi.org/10.1002/advs.201600152>.
- [15] C. Perdomo, N.T. Nguyen, Recent advances in 1D nanostructured catalysts for photothermal and photocatalytic reduction of CO₂, *Curr. Opin. Colloid Interface Sci.* 61 (2022) 101625, <https://doi.org/10.1016/j.cocis.2022.101625>.
- [16] N. Lu, M. Zhang, X. Jing, P. Zhang, Y. Zhu, Z. Zhang, Electrospon semiconductor-based nano-heterostructures for photocatalytic energy conversion and environmental remediation: opportunities and challenges, *Energy Environ. Mater.* 0 (2022) 1–27, <https://doi.org/10.1002/eeem2.12338>.
- [17] K. Lan, Q. Wei, D. Zhao, Versatile synthesis of mesoporous crystalline TiO₂ materials by monomicelle assembly, *Angew. Chem. Int. Ed.* 61 (2022) e202200777, <https://doi.org/10.1002/anie.202200777>.
- [18] Y. Luan, L. Jing, M. Xie, X. Shi, X. Fan, Y. Cao, Y. Feng, Synthesis of efficient N-containing TiO₂ photocatalysts with high anatase thermal stability and the effects of the nitrogen residue on the photoinduced charge separation, *Phys. Chem. Chem. Phys.* 14 (2012) 1352–1359, <https://doi.org/10.1039/c1cp22907a>.
- [19] H. Xiong, H. Zhou, G. Sun, Z. Liu, L. Zhang, L. Zhang, F. Du, Z.A. Qiao, S. Dai, Solvent-free self-assembly for scalable preparation of highly crystalline mesoporous metal oxides, *Angew. Chem. Int. Ed.* 59 (2020) 11053–11060, <https://doi.org/10.1002/anie.202002051>.
- [20] H. Xiong, T. Gao, K. Li, Y. Liu, Y. Ma, J. Liu, Z.A. Qiao, S. Song, S. Dai, A polymer-oriented self-assembly strategy toward mesoporous metal oxides with ultrahigh surface areas, *Adv. Sci.* 6 (2019) 1801543, <https://doi.org/10.1002/advs.201801543>.
- [21] X. Zhang, Y. Liu, L. Chen, Z. Li, W. Wu, J. Bian, L. Jing, Interface modulation of FePc/porous Ti(HPO₄)₂ Z-scheme heterojunctions with ultrafine Ag for efficiently photocatalytic CO oxidation, *Small Struct.* 3 (2022) 2200011, <https://doi.org/10.1002/ssstr.202200011>.
- [22] X. Zhang, Y. Liu, L. Chen, Z. Li, Y. Qu, W. Wu, L. Jing, Porous two-dimension MnO₂-C₃N₄/titanium phosphate nanocomposites as efficient photocatalysts for CO oxidation and mechanisms, *Appl. Catal. B: Environ.* 282 (2021) 119563, <https://doi.org/10.1016/j.apcatb.2020.119563>.
- [23] C. Liu, M. Zhang, H. Geng, P. Zhang, Z. Zheng, Y. Zhou, W. He, NIR enhanced peroxidase-like activity of Au@CeO₂ hybrid nanozyme by plasmon-induced hot electrons and photothermal effect for bacteria killing, *Appl. Catal. B: Environ.* 295 (2021) 120317, <https://doi.org/10.1016/j.apcatb.2021.120317>.
- [24] Q. Shi, Z. Li, L. Chen, X. Zhang, W. Han, M. Xie, J. Yang, L. Jing, Synthesis of SPR Au/BiVO₄ quantum dot/rutile-TiO₂ nanorod array composites as efficient visible-light photocatalysts to convert CO₂ and mechanism insight, *Appl. Catal. B: Environ.* 244 (2019) 641–649, <https://doi.org/10.1016/j.apcatb.2018.11.089>.
- [25] L. Chen, J. Lei, L. Tian, K. Deng, G. Cheng, One-pot in situ fabrication of Cu-coupled rugby-shaped BiVO₄ spherulite for enhancing photocatalytic activity with SPR effect via ultrasonic hydrothermal strategy, *Ceram. Int.* 47 (2021) 23001–23013, <https://doi.org/10.1016/j.ceramint.2021.05.014>.
- [26] C. Nie, P. Du, H. Zhao, H. Xie, Y. Li, L. Yao, Y. Shi, L. Hu, S. Si, M. Zhang, J. Gu, L. Luo, Z. Sun, Ag@TiO₂ Nanoprisms with highly efficient near-infrared photothermal conversion for melanoma therapy, *Chem. -Asian J.* 15 (2019) 148–155, <https://doi.org/10.1002/asia.201901394>.
- [27] S. Ali, Z. Li, W. Ali, Z. Zhang, M. Wei, Y. Qu, L. Jing, Synthesis of Au-decorated three-phase-mixed TiO₂/phosphate modified active carbon nanocomposites as easily-recycled efficient photocatalysts for degrading high-concentration 2,4-DCP, *RSC Adv.* 9 (2019) 38414–38421, <https://doi.org/10.1039/c9ra08286g>.
- [28] H. Lu, Y. Qu, L. Sun, X. Chu, J. Li, Y. Liu, L. Bai, L. Jing, Improved visible-light activities of rutile nanorod by comodifying highly dispersed surface plasmon resonance Au nanoparticles and hf groups for aerobic selective alcohol oxidation, *ACS Sustain. Chem. Eng.* 6 (2018) 14652–14659, <https://doi.org/10.1021/acssuschemeng.8b03222>.
- [29] J. Shi, J. Chen, G. Li, T. An, H. Yamashita, Fabrication of Au/TiO₂ nanowires@carbon fiber paper ternary composite for visible-light photocatalytic degradation of gaseous styrene, *Catal. Today* 281 (2017) 621–629, <https://doi.org/10.1016/j.cattod.2016.06.026>.
- [30] J. Hu, R. Zhao, H. Li, Z. Xu, H. Dai, H. Gao, H. Yu, Z. Wang, Y. Wang, Y. Liu, J. Han, R. Guo, Boosting visible light photocatalysis in an Au@TiO₂ yolk-in-shell nanohybrid, *Appl. Catal. B: Environ.* 303 (2022) 120869, <https://doi.org/10.1016/j.apcatb.2021.120869>.
- [31] M. Xiao, Z. Wang, M. Lyu, B. Luo, S. Wang, G. Liu, H.M. Cheng, L. Wang, Hollow nanostructures for photocatalysis: advantages and challenges, *Adv. Mater.* 31 (2018) 1801369, <https://doi.org/10.1002/adma.201801369>.
- [32] G. Li, Z. Tang, Noble metal nanoparticle@metal oxide core/yolk-shell nanostructures as catalysts: recent progress and perspective, *Nanoscale* 6 (2014) 3995–4011, <https://doi.org/10.1039/c3nr06787d>.
- [33] F. Xu, H. Tan, J. Fan, B. Cheng, J. Yu, J. Xu, Electrospon TiO₂-based photocatalysts, *Sol. RRL* 5 (2021) 2000571, <https://doi.org/10.1002/solr.202000571>.
- [34] H. Han, T. Song, J.-Y. Bae, L.F. Nazar, H. Kim, U. Paik, Nitridated TiO₂ hollow nanofibers as an anode material for high power lithium ion batteries, *Energy Environ. Sci.* 4 (2011) 4532–4536, <https://doi.org/10.1039/c1ee02333k>.
- [35] A. Zada, Y. Qu, S. Ali, N. Sun, H. Lu, R. Yan, X. Zhang, L. Jing, Improved visible-light activities for degrading pollutants on tio2/g-c3n4 nanocomposites by decorating SPR Au nanoparticles and 2,4-dichlorophenol decomposition path, *J. Hazard. Mater.* 342 (2018) 715–723, <https://doi.org/10.1016/j.jhazmat.2017.09.005>.
- [36] M.J. Hostetler, J.E. Wingate, C.-J. Zhong, J.E. Harris, R.W. Vachet, M.R. Clark, J. D. Londono, S.J. Green, J.J. Stokes, G.D. Wignall, G.L. Glish, M.D. Porter, N. D. Evans, R.W. Murray, Alkanethiolate gold cluster molecules with core diameters from 1.5 to 5.2 nm: core and monolayer properties as a function of core size, *Langmuir* 14 (1998) 17–30, <https://doi.org/10.1021/la970588w>.
- [37] Y. Wu, Y. Li, P. Liu, S. Gardner, B.S. Ong, Studies of gold nanoparticles as precursors to printed conductive features for thin-film transistors, *Chem. Mater.* 18 (19) (2006) 4627–4632, <https://doi.org/10.1021/cm0611643>.
- [38] J. Chen, G. Li, Y. Huang, H. Zhang, H. Zhao, T. An, Optimization synthesis of carbon nanotubes-anatase TiO₂ composite photocatalyst by response surface methodology for photocatalytic degradation of gaseous styrene, *Appl. Catal. B: Environ.* 123–124 (2012) 69–77, <https://doi.org/10.1016/j.apcatb.2012.04.020>.
- [39] H. Shan, Y. Si, J. Yu, B. Ding, Facile access to highly flexible and mesoporous structured silica fibrous membranes for tetracyclines removal, *Chem. Eng. J.* 417 (2021) 129211, <https://doi.org/10.1016/j.cej.2021.129211>.
- [40] J. Chen, Z. He, Y. Ji, G. Li, T. An, W. Choi, OH radicals determined photocatalytic degradation mechanisms of gaseous styrene in TiO₂ system under 254 nm versus 185 nm irradiation: combined experimental and theoretical studies, *Appl. Catal. B: Environ.* 257 (2019), <https://doi.org/10.1016/j.apcatb.2019.117912>.
- [41] L. Chen, X. Niu, Z. Li, Y. Dong, D. Wang, F. Yuan, Y. Zhu, The effects of BaO on the catalytic activity of La_{1.6}Ba_{0.4}NiO₄ in direct decomposition of NO, *J. Mol. Catal. A: Chem.* 423 (2016) 277–284, <https://doi.org/10.1016/j.molcata.2016.07.022>.
- [42] N. Zhang, C. Han, X. Fu, Y.-J. Xu, Function-oriented engineering of metal-based nanohybrids for photoredox catalysis: exerting plasmonic effect and beyond, *Chem* 4 (2018) 1832–1861, <https://doi.org/10.1016/j.chempr.2018.05.005>.
- [43] J. Chen, Z. He, G. Li, T. An, H. Shi, Y. Li, Visible-light-enhanced photothermocatalytic activity of ABO₃-type perovskites for the decontamination of gaseous styrene, *Appl. Catal. B: Environ.* 209 (2017) 146–154, <https://doi.org/10.1016/j.apcatb.2017.02.066>.
- [44] C. Pan, C. Wang, X. Zhao, P. Xu, F. Mao, J. Yang, Y. Zhu, R. Yu, S. Xiao, Y. Fang, H. Deng, Z. Luo, J. Wu, J. Li, S. Liu, S. Xiao, L. Zhang, Y. Guo, Neighboring sp-hybridized carbon participated molecular oxygen activation on the interface of sub-nanocluster CuO/graphdiyne, *J. Am. Chem. Soc.* 144 (2022) 4942–4951, <https://doi.org/10.1021/jacs.1c12772>.
- [45] L.F. Bobadilla, J.L. Santos, S. Ivanova, J.A. Odriozola, A. Urakawa, Unravelling the role of oxygen vacancies in the mechanism of the reverse water–gas shift reaction by operando drifts and ultraviolet-visible spectroscopy, *ACS Catal.* 8 (2018) 7455–7467, <https://doi.org/10.1021/acscatal.8b02121>.

- [46] Q. Li, C. Wu, K. Wang, X. Wang, X. Chen, W. Dai, X. Fu, Comparison of the catalytic performance of Au/TiO₂ prepared by in situ photodeposition and deposition precipitation methods for CO oxidation at room temperature under visible light irradiation, *Catal. Sci. Technol.* 12 (2022) 237–249, <https://doi.org/10.1039/d1cy01829a>.
- [47] S. Gaur, H. Wu, G.G. Stanley, K. More, C.S.S.R. Kumar, J.J. Spivey, CO oxidation studies over cluster-derived Au/TiO₂ and aurolite™ Au/TiO₂ catalysts using drifts, *Catal. Today* 208 (2013) 72–81, <https://doi.org/10.1016/j.cattod.2012.10.029>.
- [48] T. Xu, X. Liu, T. Zhu, C. Feng, Y. Hu, M. Tian, New insights into the influence mechanism of H₂O and SO₂ on Pt–W/Ti catalysts for CO oxidation, *Catal. Sci. Technol.* 12 (2022) 1574–1585, <https://doi.org/10.1039/d1cy01984h>.